D2.2 RANS-based simulations with meteorological and geometrical uncertainty quantification

Date: Mar 24, 2025

Funded by
the European Union

This Project has received funding from the European Union's HORIZON Research and Innovation Programme under Grant Agreement number 101096698

Document Identification			
Status	Final	**Due Date**	31/03/2025
Version	0.1	**Submission Date**	24/03/2025

Related WP	WP2	**Document Reference**	D2.2
Related Deliverable(s)	Task 2	**Dissemination Level (*)**	PU/CO/CI/Int
Lead Participant	Akshay Patil & Clara García-Sánchez (TUD-BK)	**Lead Author**	Akshay Patil
Contributors	Gerardo Zampino (KTH)	**Reviewers**	Clara García-Sánchez, TUD-BK
			Gerardo Zampino, KTH

Keywords:
Reynolds-Averaged Navier-Stokes, Urban Fluid Dynamics, OpenFOAM, Level of Detail (LoD)

Document Information

List of Contributors	
Name	**Partner**
Akshay Patil	TUD
Clara García-Sánchez	TUD
Gerardo Zampino	KTH

Document History			
Version	**Date**	**Change editors**	**Changes**
0.1	05/03/2025	Akshay Patil (TUD)	Initial Draft
0.2	21/03/2024	Akshay Patil (TUD)	Revision #1
1.0	24/03/2025	Akshay Patil (TUD)	Final Version

Quality Control		
Role	**Who (Partner short name)**	**Approval Date**
Deliverable leader	Clara García-Sánchez (TUD)	24/03/2025
Quality manager	Clara García-Sánchez (TUD)	24/03/2025
Project Coordinator	Ricardo Vinuesa (KTH)	26/03/2025

Table of Contents

List of Tables

List of Figures

List of Acronyms

Abbreviation / acronym	Description
CFD	Computational Fluid Dynamics
Dx.y	Deliverable number y belonging to WP x
EC	European Commission
GCI	Grid Convergence Index
KNMI	Koninklijk Nederlands Meteorologisch Instituut
LoD	Level of Detail
RANS	Reynolds Averaged Navier Stokes
TUD	Delft University of Technology
W.R.T	With Respect To
WP	Work Package

Executive Summary

Wind flow predictions in realistic urban areas are sensitive to a wide range of governing parameters such as building geometry, wind incidence, urban morphology, and underlying topography, to list a few. Often, the direct influence of these independent parameters is difficult to quantify given the large range of values they can take, consequently, limiting a systematic evaluation of their effect on the parameter of interest i.e., the wind flow. This task focused on developing a Reynolds-Averaged Navier-Stokes (RANS) computational framework to better understand and quantify the effect of one of the parameters, namely, the geometric resolution of the built environment through the use of levels of detail (LoD).

Leveraging a probabilistic risk metric (P_r) based on velocity and turbulence fields, a systematic comparison between LoD1.2 and LoD2.2 (low and high geometry detail reconstruction level) in two different urban settings: the TUD-campus (fairly open with varying height buildings) and Den Haag centrum (compact with similar height buildings). The findings suggest that LoD2.2 provides a more conservative prediction for high-risk areas compared to LoD1.2. Our results and methodology can help better predict the risk associated with urban air mobility and wind engineering applications with the appropriate tuning of the risk metrics for the requisite of application.

2. Introduction

The need for understanding the impact of wind prediction in the urban built environment has accelerated in recent years to envision, improve, and support the development of sustainable and climate-conscious urban planning [1]. The disproportionate concentration of economic and social activities and infrastructure within the urban built environment in almost all major urban centres in the world has imparted a unique resource-strain on the modern urban built environment. As urban centres in the world take up more land to accommodate for the increasing population density [2-3], complex and archaic zoning laws coupled with the limited horizontal space has led to the growth of taller buildings in urban areas, thus exacerbating wind-comfort and peak wind loading [4-7]. In addition to wind comfort, air quality (specifically SO_2 and NO_x) globally became progressively worse until 2018 [8], at which point concrete emissions control was undertaken to improve the air quality in urban areas. Wolf et al. [9] conducted a high-resolution study in the city of Bergen, Norway, and found that poor urban air quality and particulate matter ($PM_{2.5}$) can be attributed primarily to road traffic. Another study commissioned by the European parliament found similarly concerning levels of air quality in urban environments [10] and recently lowered[1] the permissible levels for particulate matter, SO_x, NO_x, and O_3, illustrating a pressing need to better understand, predict, and combat these situations.

One potential solution to alleviate the poor air quality in urban areas that has been proposed is to eliminate traditional last-mile transit modes and supplement these with Unmanned Aerial Vehicles (UAV) [11-12]. Here, last-mile transit refers to the modes of transportation that use diesel/petrol vehicles when inside the city centre which adds to a lot of CO_2, SO_x and NO_x type pollution. Since urban areas are dense canopies, this aggravates the issue where the pollution stays inside the city centre. Lemardele et al. [13] explored various UAV last-mile transit options to quantify the financial feasibility of using air delivery coupled with a traditional transit option in European cities like Barcelona, Spain and Paris, France. One of the significant factors in deciding the viability of such a drone delivery system in dense urban areas was the incident wind conditions that can severely affect the battery drain rate for small- to medium-sized UAVs [14]. Moreover, they found that statistically characterising the potential risk of traversing a given neighbourhood can provide substantial benefits when deciding the route. Predicting the wind conditions in a complex urban environment involves many challenges that have been concisely summarised by Blocken [15]. Understanding the response of the urban environment to changing boundary conditions (in this case,

[1] European Comission, Council of the European Union. https://www.consilium.europa.eu/en/press/press-releases/2023/03/28/fit-for-55-council-adopts-regulation-on-co2-emissions-for-new-cars-and-vans/pdf/

wind-incidence angle) is still poorly understood due to the wide variety of urban morphology. In this case, the definition of urban morphology is confined to the spatial context as discussed in [16-18] where the urban form does not constitute a single metric but a collection of multiple metrics, including the layout of the street network, building heights, building cluster, to list a few of as many as 300 metrics [18] used to define the urban form/morphology.

Several past studies [19-21] have been carried out focusing on the effect of geometry acquisition, wind-incidence angle resolution, and the effect of urban morphology to recommend the FKB (national general feature catalogue of Norway) database model for geometry acquisition. The research suggests that a minimum of 36 wind directions might be enough to predict the pedestrian wind comfort classes, neglecting the effect of urban morphology on wind prediction capabilities. In one study, the authors [19] compare the wind-comfort classification without including semantic surfaces, which are known to affect the flow above them critically. While having an average roughness characteristic of the underlying terrain can provide suitable predictions, not including semantic surfaces such as water, vegetation, and forest, to list a few, can substantially miss the local zones of accelerations/decelerations, thus providing problematic wind-comfort classifications [22-24]. Additionally, while the building acquisition method provides a harmonised approach in the methodology for identical point clouds, the reconstruction of the building geometry and its accuracy cannot be ensured, thus introducing arbitrary geometric detail when making such a comparison. In this case, the same point cloud can yield a varying level of geometric detail and substantially influence the wind prediction capabilities [23,25].

Furthermore, the fact that only four wind directions can classify the wind-comfort maps (derived from velocity magnitude) with approximately 79% accuracy when compared to 64 wind directions [20] begs the question of whether the wind-comfort maps provide an accurate representation of the flow dynamics within the urban environment. While Hagbo et al. [21] suggest that urban morphology does not dictate the classification of the wind-comfort in urban areas, the metrics used to define urban morphology are not representative of the overall complexity observed in the broader set of urban areas [18,26]. This is especially true when preferential wind directions are considered through a non-uniform windrose, where the effect of urban morphology can become more pronounced. A wide range of studies have explored the effect of varying urban density, plan area density, frontal area density, varying ratios of urban canyons, building height and aspect ratios, to list a few, to find systematic flow response differences subject to varying parameters [27-30]. However, as discussed earlier, accurately characterising the various metrics that go into the definition of urban

morphology can easily exceed approximately 300 parameters [18] and even a straightforward assumption that about 5% of these parameters contribute at the first-order level would require at least 15 parameters to be included in understanding the flow response. Consequently, a fair comparison of the effect of urban morphology would require a strict definition of what constitutes urban morphology. While a harmonised definition of urban morphology leads to a large parametric space, one relevant metric that can provide a consistent way to differentiate the built environment (i.e., buildings) is the Level of Detail (LoD) [31]. The central utility of such a standard definition of LoD is that it allows for unambiguous characterisation of the buildings. Each successive LoD refinement leads to a distinct geometry asymptotically converging to the actual building. This allows for systematically differentiating the built environment [31] for wind simulations and potentially other applications of interest. It must be noted that despite such a concise definition, a recent study by van der Vaart et al. [32] found some deficiencies in this definition of LoD and have since been expanded to accommodate additional metrics and variations mainly dealing with additions to LoD2.2 or higher. Despite these limitations, as detailed in Biljecki et al. [31], the LoD definition still provides a consistent method for urban fluid dynamics applications as considered in this work.

2.1 Purpose of the document

As detailed in the motivation, predictive capabilities using a computationally efficient and relatively fast method can act to provide a first prediction of the anticipated risk associated with routing and planning UAV trajectories in complex urban areas. Consequently, we designed the simulation framework that accommodates complex urban areas (Delft university campus and the city of Den Haag) to generate a dataset that illustrates how relatively simple CFD models can be used to predict the associated risk using a probabilistic framework. In this document we detail how the simulations can be used in a predictive capacity for informing the connected work packages to make relatively cost-effective decisions.

2.2 Relation to other project work

The low-fidelity results have the unique advantage of simulating geometry resolved wind simulations around complex urban built environment for in-situ wind and modelled turbulence conditions. The results and methodology discussed in this deliverable will be used in the final prototype delivery in WP5 as well as in the WP6 that aims to showcase the results and the data. Potential application for WP3, where trajectory optimization strategies are explored and deployed, can also be applied with the data provided by the current effort.

2.3 Structure of the document

In the rest of the document, we will present 3 chapters as detailed below:

Chapter 3: Computational Framework and Simulation Description

Chapter 4: Results and Discussions

Chapter 5: Concluding Remarks and Recommendations

3 Computational Framework and Simulation Description

3.1 Governing equations and discretization

In this work we use the steady-state Reynolds-averaged Navier-Stokes (RANS) momentum equations constrained by the incompressible flow assumption to obtain the wind field within the urban environment. The governing equations are given by

$$\partial_m \overline{u_m u_n} = -\frac{1}{\rho}\partial_n \bar{p} + \nu \partial_m \partial_m \overline{u_n} + \partial_m \overline{u'_m u'_n} \quad (1)$$

and

$$\partial_m \overline{u_m} = 0 \quad (2)$$

where ρ is the density of the fluid, which is assumed to constant, ν is the kinematic viscosity of the fluid ($\nu_{air} = 10^{-5}\frac{m^2}{s}$), $\overline{u_n}$ represents the Reynolds-averaged velocity, $\bar{p}$ is the Reynolds-averaged pressure, and $\partial_m \overline{u'_m u'_n}$ are the Reynolds-stress', that constitute the closure problem for incompressible fluid flow equations described in equations (1) and (2) where u'_n represents the fluctuating component of the velocity. In the equations above, we use the tensorial index notation, where repeating indices are summed over unless mentioned otherwise. The system of equations is mathematically closed using the Boussinesq eddy-viscosity hypothesis that relates the Reynolds-stress to the mean rate of strain via the linear eddy viscosity using the $k-\epsilon$ turbulence closure equation [33], where $k = \frac{\overline{u'_n u'_n}}{2}$ is the turbulent kinetic energy (TKE) and $\epsilon = \nu \overline{\partial_m u'_n \, \partial_m u'_n}$ is the TKE dissipation rate. Specifically, the standard variant [33] of the two-equation closure is used to solve the transport equations given by

$$\partial_m k\, \overline{u_n} = \partial_m \left(\nu + \frac{\nu_t}{\sigma_k}\partial_m k\right) + P_k - \epsilon + S_k, \quad (3)$$

and

$$\partial_m \epsilon \overline{u_n} = \partial_m \left(\nu + \frac{\nu_t}{\sigma_\epsilon}\,\partial_m \epsilon\right) + C_{1,\epsilon} S_\epsilon - \frac{C_{2,\epsilon}\epsilon^2}{k+\sqrt{\nu\epsilon}} + S_\epsilon, \quad (4)$$

where equations 3 and 4 are the transport equations for k and ϵ, respectively. Here $\sigma_k = 1.0, \sigma_\epsilon = \frac{1}{3}$, $C_{1,\epsilon} = 1.44$, and $C_{2,\epsilon} = 1.92$ are the model constants that have an empirical origin to close the transport equations for k and ϵ. While P_k is the production of TKE, S_k is the sink of TKE, and S_ϵ is the sink term for TKE dissipation rate. The turbulent/eddy-viscosity (ν_t) is computed as

$$\nu_t = \frac{C_\mu k}{\epsilon}, \quad (5)$$

where C_μ constitutes the model coefficient.

The governing equations are discretised in space using a second-order accurate, collocated finite-volume method, while the pseudo-time stepping is used through the Semi-Implicit Method for Pressure Linked Equations (SIMPLE) algorithm to integrate the steady-state equations [34]. The governing equations are solved using the MPI-parallelised computational toolbox OpenFOAM (version 7) [35]. The steady-state solutions are integrated for a total of 3500 iterations until the normalised-residuals plateau for the pressure-solver at around 10^{-3}, and those for velocity and the two scalars reach $\sim 10^{-5}[1]$. All the simulations are run using the Delft Blue super-computing centre [36] at the Delft University of Technology, Delft, using Intel Xeon E5-6448Y CPUs with 64 cores. Each simulation takes approximately 576 CPU hours to obtain converged solutions, requiring approximately 68 GiB of memory and generating a maximum of 5 GiB of data containing the 3D snapshots for velocity, pressure, and three scalars corresponding to the turbulence closure.

3.2 Mesh design and grid convergence

To simulate flow around a realistic urban area, we choose the Delft University of Technology campus (henceforth TUD-campus) and the city of Den Haag (henceforth the Hague) as representative urban areas in terms of the built environment as they showcase a variety of buildings, vegetation, water bodies, and other semantic surfaces that are in a single area. For the TUD-campus case, only the central part of the university campus is considered. The faculties of aerospace and applied sciences are not included as they are relatively far away from the central campus and including them would add substantial computational costs. The proximity of the two urban areas to a wind measurement station allows for the leveraging of incident wind conditions that can be used as boundary conditions for setting up the model.

Figure 1 depicts the choice of the urban area and the computational mesh as discretised in the numerical framework used in this study. The building geometry for LoD2.2 is obtained from the 3DBAG database [37] while LoD1.2 buildings are directly reconstructed using City4CFD [38,39]. Surface features such as terrain, vegetation, and water polygons are obtained from the Dutch national digital repository of geospatial data2. These two tools allow for seamless integration of the building environment into the computational mesh in an automated workflow, ensuring that all the semantic surfaces, such as terrain, water, and vegetation, can be correctly incorporated along with the buildings in the region of interest. The total time, including data acquisition, curation, and reconstruction required to generate the input geometry for the TUD-campus and The Hague cases, was approximately 2 hours. Here, the time

[2] https://www.pdok.nl/

required to carry out the reconstruction of the buildings and semantic surfaces in City4CFD is in the order of a hundred seconds, while most of the time is spent in preparing the data in QGIS3. Figure 1(b) and Figure 1(d) show the buildings are accurately placed along with the other surfaces thus improving the representation of the various elements present in the urban environment. Using the updated Davenport roughness classification [40], [41], the surface roughness parameter is prescribed according to surface classification, to capture the influence of different terrain features.

The flow domain is designed following the best practice guidelines as detailed in [1], [42] using a cylindrical domain around the region of interest as shown in Figure 1.The cylindrical domain enables running various inflow directions without discretizing the domain for every wind incidence angle. To carry out the grid convergence/sensitivity test, we use the TUD-campus case with a wind incidence angle of $\theta = 210°$ w.r.t the North. A similar grid convergence test was carried out for the Hague case but has not been detailed here for brevity. Table 1 details the three meshes considered in the grid convergence test where the representative grid size is the average grid size computed as

$$\Delta h_r = (\overline{\Delta V})^{\frac{1}{3}}, \tag{6}$$

where $\overline{\Delta V}$ is the average cell volume in the domain. As the flow field around the urban area is relatively complex, to avoid contamination of grid sensitivity estimates due to local grid effects, we sample approximately 200 probes and 100 line probes as shown in Figure 2 within the domain and use the median grid convergence index (GCI) parameter [43] to estimate the suitability and grid independence for this case.

Mesh Name	Number of Cells ($\times 10^6$)	Smallest Cell Height Δh (m)	Representative Grid Size Δh_r (m)
Coarse	9.6	0.104	12.46
Nominal	22.35	0.056	8.92
Fine	46.61	0.041	7.22

Table 1: Description of the three grids used to understand the sensitivity of the mesh to understand the sensitivity of the mesh to the predicted results.

As shown in Figure 2(b), there is very little difference observed between the velocity profiles across all the mesh sizes, and this is consistent for the other 96-line probes sampled (not shown here) in the comparison. Some differences were observed in the lower portions of the velocity profiles. However, the differences were insignificant, and there was monotonic convergence towards the fine mesh results.

[3] https://www.qgis.org/

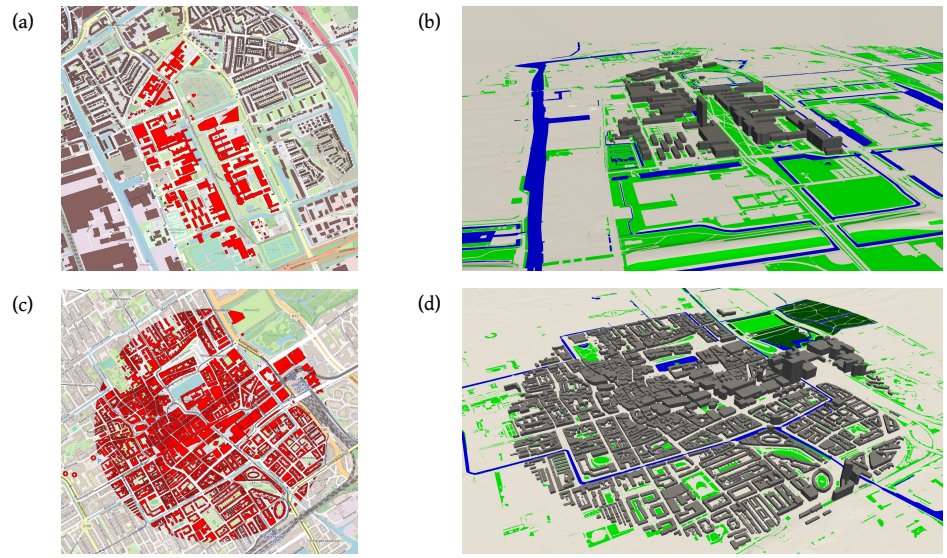

Figure 1: (a) and (c) Map of the region of interest relative to the other features with the red polygons indicating the built environment that is considered in this study. Figure courtesy of Open Street Map4. (b) and (d) Computational mesh (LoD 1.2) depicting the buildings and the terrain used in the study to simulate the urban environment. Buildings are marked by grey, vegetation is marked by green, forest in dark green, ground/terrain is marked by white, and water is marked by blue.

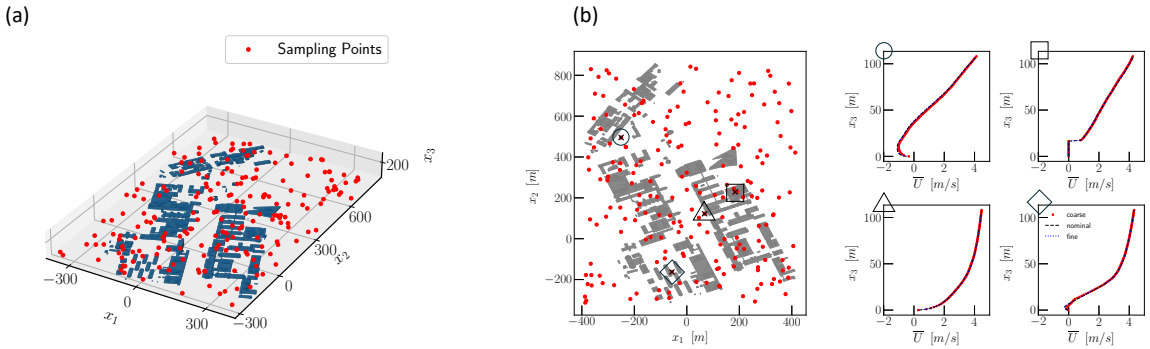

Figure 2: (a) 3D rendering of the buildings along with the 200 sampling probes used to study the grid convergence for the grid sizes mentioned in . The blue regions mark the buildings, while the red dots indicate the locations where all flow parameters are sampled. (b) The top view of the buildings is marked in grey, and the vertical line sampling probe locations are marked in red. Four panels on the right compare the velocity profiles at various different locations corresponding to the symbol marked at the top right corner of each sub-panel.

[4] https://www.openstreetmap.org

The median value of the apparent order of convergence is higher than the discretization order of convergence due to similar results obtained on all three meshes. The rest of the three parameters are all below 3% and suggest that the results obtained are sufficiently grid-independent. As a result, the nominal mesh will be used for all the results discussed in the following section as it is sufficiently accurate and computationally efficient based on the metrics presented in Table 2.

Parameter	$\overline{U_1}$	$\overline{U_2}$	$\overline{U_3}$	$\overline{p}$	k	ϵ
Apparent Order	4.4	4.4	4.1	4.7	3.0	4.6
Relative Error (%)	0.18	0.15	2.1	1.42	0.61	1.0
Extrapolation Error (%)	0.14	0.13	1.94	0.9	0.9	0.7
GCI (%)	0.18	0.17	2.44	1.12	1.13	0.85

Table 2: Grid convergence indicators for the three meshes used to test the sensitivity of the grid on the results predicted. Since the turbulent eddy viscosity (ν_t) is a derived parameter, it has not been included in the table above.

Since the flow conditions for LoD2.2 are identical to those considered for LoD1.2, the mesh design for LoD2.2 is based on the geometric resolution requirements. As the building features for LoD2.2 are relatively more complex when compared to those of LoD1.2 [31], a finer grid resolution is required for LoD2.2 to resolve these small geometric details. Consequently, for LoD2.2, the computational grid has approximately 48 million cells. Similar differences between the two LoDs were observed for the Hague case, where LoD2.2 required a finer grid resolution than LoD1.2. Effectively, this requires an additional computational cost of 1.5 times for the LoD1.2 cases. It is also important to remark that this increased cost is expected to be non-linear and is sensitive to the computational framework used and its weak-scaling behavior; since OpenFOAM scales approximately linearly for the problem sizes considered in this work, there are no substantial parallelization costs associated when comparing LoD1.2 and LoD2.2 for the hardware on which these simulations are run.

3.2 Wind Characteristics

To characterize the wind conditions for the TUD-campus case, we use the weather station data collected by the Delft University of Technology accessed through the

weather data platform[5]. Specifically, we use the Delfshaven weather station to characterise the wind data to supply the simulation boundary conditions in this paper. As for the Hague case, data from the KNMI data portal[6] was processed for the Voorschoten weather station. Figure 3 shows the normalised wind rose for both weather stations over twenty years 2002 until 2022. Panel (a) shows the normalised wind-rose for the Delfshaven stations with a 1° resolution. For the TUD-campus, most of the incident wind comes from the west, while for the Hague case, most of the incident wind originates in the south (not shown here). The wind histogram shown in Figure 3(b) follows a log-normal distribution marked by the solid black line. Since we are interested in understanding the average/mean wind conditions in this study, the black dotted line with an x marks the wind speed location chosen as the simulation's representative inflow boundary condition. For the Hague case, the same wind condition corresponds to the mean wind conditions. However, it is important to realise that the KNMI data is measured at 10m above the ground. At the same time, the Delfshaven measurement station is located approximately 4m above the ground, thus explaining the difference between the two stations. In our simulations, we consider the 10m representative velocity at the inflow boundary condition, which corresponds to the 5m/s choice made for the simulations. In this study, increments of 1° are made for the inflow angle to span the entire wind-rose over 360°, consequently, only the wind direction is changed while the inflow velocity magnitude is fixed.

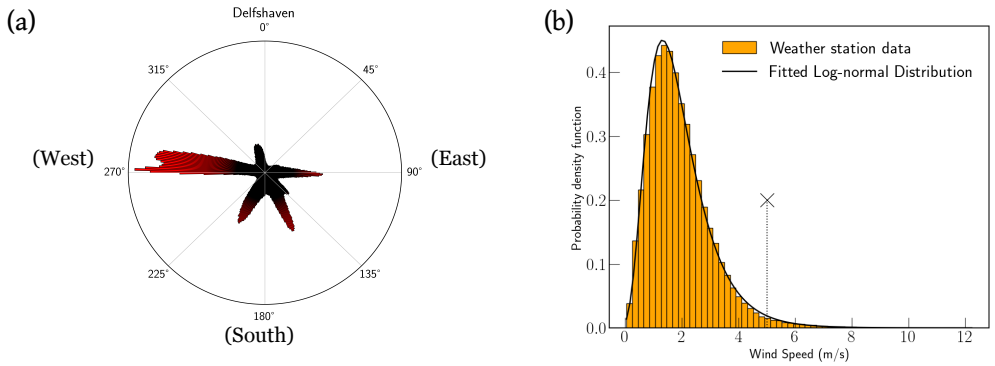

Figure 3: (a) Twenty-year averaged (2002 to 2022) and normalised wind-rose diagram for Delfshaven Wind-speed probability density function (PDF) for Delfshaven measurement station. (b) Fitted log-normal distribution marked using the black solid line. The black dashed line and cross mark the inflow velocity chosen for the simulations.

[5] https://weather.tudelft.nl/
[6] https://www.knmi.nl/nederland-nu/klimatologie/daggegevens

4 Results & Discussions

4.1 TUD-campus case

We start by first presenting the wind-rose weighted average quantity defined as

$$\overline{f_a} = \frac{1}{N_\theta} \sum_{i=1}^{i=N_\theta} w_i |\, f_i \,|, \tag{7}$$

where N_θ are the number of wind-incidence angles simulated, w_i is the weight which is the normalised value of the wind-rose pdf for angle θ_i, and $|f_i|$ is the L_2-norm if f is a vector quantity or the scalar magnitude otherwise, at a given grid-point. Figure 4 shows the non-dimensional $\overline{U_a}$ comparison at five different vertical heights for the two LoDs considered in this study (i.e., LoD1.2: lower geometric detail and LoD2.2: higher geometric detail). Good agreement between both the LoDs can be seen when comparing Figure 4(a) and Figure 4(b) within the region of interest where the peak wind magnitude is within 5% when comparing the two LoDs. The hot-spot for large wind velocity approximately at the $(x_1 \sim 50, x_2 \sim 0)$ coordinates suggests that both the LoDs can capture the location and magnitude relatively accurately. For the LoD2.2 case where the tall building located at $(x_1 \sim 0, x_2 \sim -50)$ has a characteristic difference in its dimensions when compared to the LoD1.2 scenario, the region with a significant value of $\overline{U_a}$ is observed to be offset away from the adjacent buildings and towards the south-east quadrant in the figure. Since LoD1.2 attributes a uniform height of the building to the entire footprint, the flow is artificially strained in the lateral direction, leading to large wind velocity when compared to the LoD2.2 scenario, where such straining is not as severe, thus shifting the peak both in location and magnitude. Despite the shortcomings observed in LoD1.2 compared to LoD2.2, as shown in Figure 4, the regions of high-wind speed are adequately addressed.

For safe UAV operations, knowing the locations of high-wind speed is not sufficient as it does not provide a valuable metric for other unsteady processes that may be present; this is especially true for a steady-state RANS simulation where such unsteady features are absent as detailed in equation 1. Consequently, to understand the risk associated with UAV operations, a probabilistic framework must be considered where the high-wind speed regions conditioned on large TKE regions can be used to create a risk map as a function of space. Additionally, looking at the velocity or the TKE levels independently can result in diverging conclusions. This metric is motivated by different-sized UAVs interacting differently with the flow around them. The term risk here is used in the broadest sense and can be referenced as predicted risk potential. To this end, we consider the risk map, which is defined as the probability given by

$$P^r \equiv P(u^* > \alpha \cap k^* > \beta), \tag{8}$$

where P^r is the join probability that the non-dimensional velocity $u^* \equiv \frac{U}{U_\infty}$ exceeds a given value α and the non-dimensional TKE $k^* \equiv \frac{k}{U_\infty^2}$ exceeds a value β, where both α and β are defined constants. These constants are functions of the urban morphology and require an

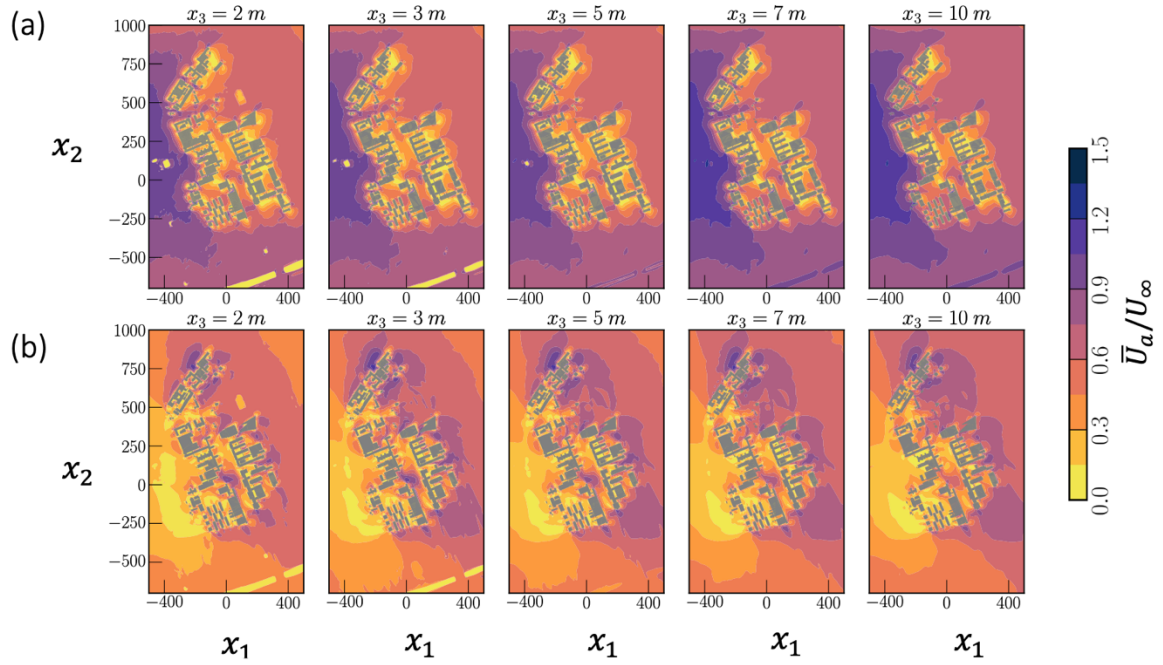

Figure 4: (a) Non-dimensional wind-speed for LoD 1.2 where the dark shades mark larger wind-speed while lighter shades mark low wind-speed. Here $U_\infty = 5$m/s, which is the wind speed at the inflow boundary condition. (b) Same as row (a), except that this row corresponds to building LoD 2.2. The empty white regions correspond to terrain where data is not represented as it is $\overline{U_n} = 0$ due to the no-slip boundary condition.

understanding of how the flow is expected to respond to a given urban morphology. For example, for heterogeneous urban areas, the flow within the urban canopy is expected to have relatively larger energy dissipation and thus lower levels of U^* and k^* and vice-versa for non-heterogeneous urban areas. Additionally, since different-sized UAVs interact with the flow around them differently, α and β can be set based on the UAV characteristics and expected flow levels, as discussed earlier. Consequently, in our case, unless otherwise specified, we use $\alpha = 0.4$ and $\beta = 0.08$ for all the discussion relating to the risk map P^r. For UAV applications, we consider the 7m and 10m above the ground as representative heights for wind speed within the urban environment.

Figure 5 shows the risk map comparison for the two LoDs considered in this study.

Despite the relatively good comparison for the wind speed in Figure 4, the risk map clearly shows some deficiencies when directly comparing the bulk parameters for two different LoDs. In this case, there is quite a large discrepancy observed between LoD1.2 and LoD2.2 for $P^r = 0.5$, which can be interpreted as a 50% chance that both the mean velocity and the TKE levels exceed the threshold's ($\alpha = 0.4$ & $\beta = 0.08$). Large differences are observed in regions with flow separation and canyon-like regions where the mean flow is strained. Since identical turbulence closure and wind incidence conditions are used, these differences can be attributed to the difference in the geometric resolution, i.e., LoD. While the risk map in Figure 5 is shown in two dimensions, a 3-dimensional risk map (perhaps more aptly field) can also be estimated, and regions of large P^r can be identified to inform UAV trajectory planning and routing. In this case, the region would constitute iso-surfaces as opposed to iso-contours such as the ones shown here; however, for the sake of brevity, the iso-surface for high-risk regions has not been presented in this section. Despite the lack of any unsteady features in the results discussed thus far, the risk map serves as a first indicator which can be used to identify potentially problematic regions where a more informed trajectory decision can be made using unsteady/real-time sensed data.

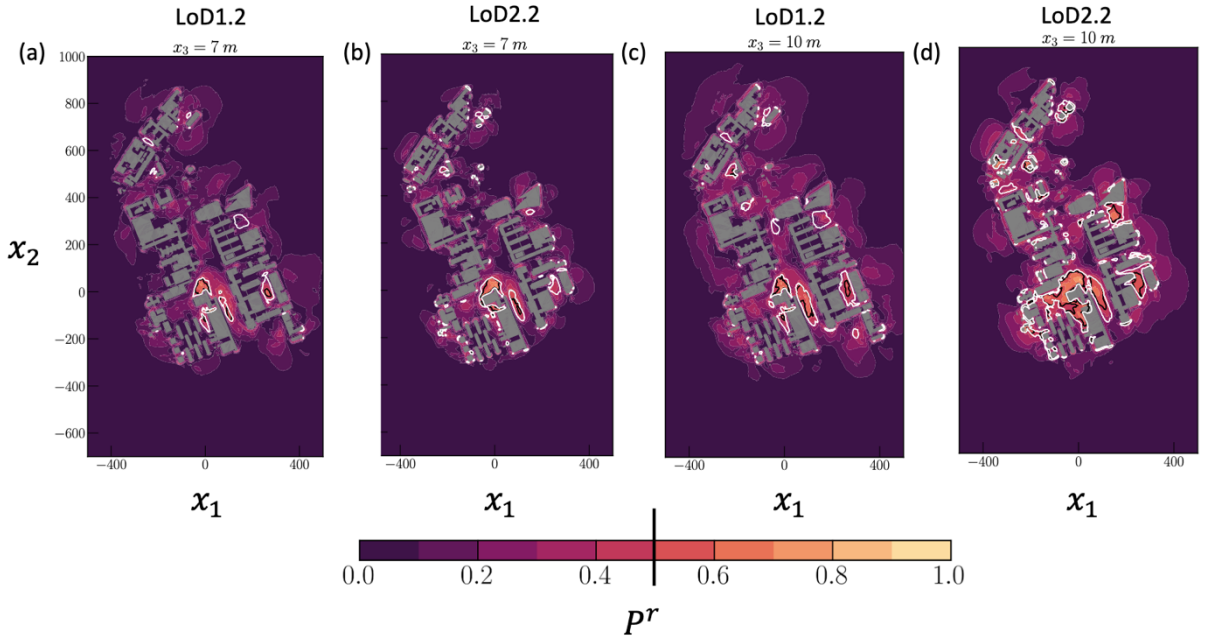

Figure 5: Comparison of the risk metric as a function of the two LoDs considered in this study at 7m and 10m above the ground ($x_3 = 0$). Here, the solid black line marks the contour for $P^r = 0.5$, and the solid white line marks the contour for $P_k^r = 0.5$, which is the probability that $k^* > \beta$.

4.2 The Hague case

The area of interest in the Hague case has a substantially different urban morphology when compared to the TUD-campus case. Specifically, the built environment has a traditionally compact arrangement as opposed to the relatively sparse built environment observed in the TUD-campus case. As shown in Figure 6, in some locations of the region of interest, a consistent over-prediction can be observed for LoD1.2 compared with LoD2.2. This over-prediction mainly seems to overestimate the total region that experiences a high wind speed for LoD1.2 due to its attribution of a single height per footprint polygon [31]. For the slice at $x_3 = 2$m in panel (a), both the low-speed and high-speed regions are relatively well captured by LoD1.2 and LoD2.2. At the same time, most of the differences are observed at the semantic surfaces, such as water and vegetation, between the two LoDs for high-speed regions. In the city center, approximately at $x_1 \sim 40$m and $x_2 \sim -10$m where there is a four-way pedestrian intersection, LoD1.2 wind predictions are observed to be relatively conservative (5% higher) when compared to that of LoD2.2. Note that LoD1.2 predicts a larger extent and more intense high-speed region. Similar observations can be made for the various x_3 locations where the comparison between LoD1.2 and LoD2.2 is similar for the wind-rose weighted speed prediction. Overall, minor differences are observed across the region of interest when comparing the two LoDs, suggesting that for the wind-rose weighted speed, the two LoDs do not exhibit significant differences similar to the TUD-campus case. These results also indicate the importance of using semantic surfaces to represent the various elements of the urban fabric, such as water, vegetation, and forest, that can be observed to have a large impact on the wind speeds observed in these regions.

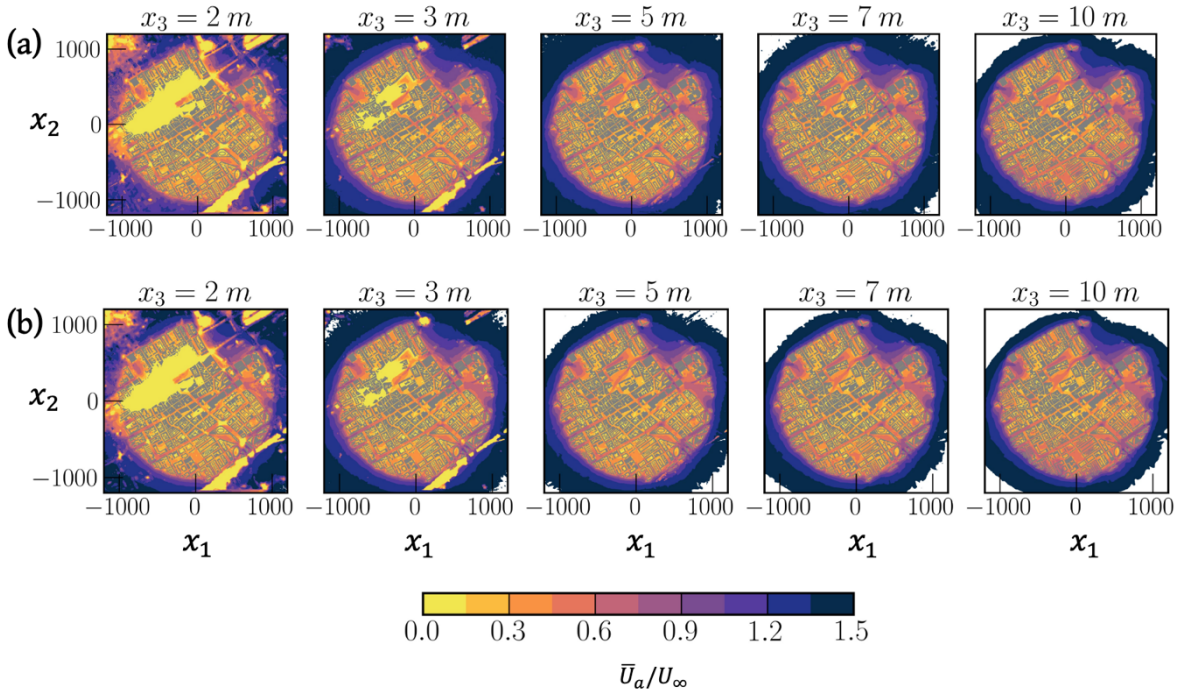

Figure 6: (a) Non-dimensional wind-speed for LoD 1.2 where the red colours mark larger wind-speed while blue colours mark low wind-speed. Here $U_\infty = 5.0\ m$/s, which is the wind speed at the inflow boundary condition. (b) Same as row (a), except that this row corresponds to LoD 2.2.

For the Hague case, the joint probability exceedance parameters are defined to be $\boldsymbol{\alpha} = \mathbf{0.4}$ and $\boldsymbol{\beta} = \mathbf{0.05}$ and Figure 7 shows the risk map for this case. Comparing LoD1.2 against LoD2.2, there is clear evidence that despite an overall larger mean wind speed prediction in both extent and magnitude, the joint probability of both the wind speed and the turbulence level is consistently under-predicted when using LoD1.2. This joint probability definition differs from the comfort class **categorization** [44] that is only conditioned on wind speed. It is clear from the trend that the locations of high wind speed are a sub-set of high turbulence levels based on the fact that the black contour lines are enveloped by the white contour lines in Figure 5and Figure 7. The information about high turbulence levels is essential in the case of UAVs, given that the relevant gradients are proportional to the size of the UAV, and this information can be extracted from the turbulence levels. While LoD1.2 can capture the risk regions (defined in equation 8), there is a systematic under-prediction of the extent and the risk magnitude associated. These observations collectively suggest that using a probabilistic metric conditioned only on the wind speed can provide a false sense of similarity where the effect of the geometric detail can seem less important when, in reality, substantial differences exist in the data. Since building height constitutes one metric in the urban morphology characterisation [18,26] and the attribution of building height is dependent on the LoD classification [31,45], it is important to correctly isolate the effect of such a

systematic building characterisation in urban fluid dynamics applications. Specifically, when using mixed LoD building models, the impact of LoD can become substantially large depending on the parameter of interest, and a generalised conclusion of the effect of such a characterisation should be made with caution.

Since the risk map as presented in the above two sub-sections exhibits substantial variations when the two LoDs are compared, we also carried out a systematic sensitivity analysis for the threshold values. Specifically, we considered $\alpha = [0.1, 0.2, 0.3, 0.4, 0.5, 0.6, 0.7]$ and $\beta = [0.03, 0.04, 0.05, 0.06, 0.07, 0.08, 0.09, 0.1]$ resulting in a total of 56 different combinations of the exceedance parameters to better understand the behaviour of the risk map subject to the two parameters. For a detailed discussion, the readers are referred to Annex A of this report. In summary, we observe that for small values of the α it is difficult to draw precise conclusions as the entire area of interest is classified as a high-risk region, which is not surprising. While cases with increasing values of α, LoD1.2 are observed to be consistently under-prediciting the risk region. It is clear from this discussion that spanning the 300 or so metrics using a computational fluid dynamics (CFD) approach is not feasible for producing engineering solutions. This is true even for a simplified Reynolds-Averaged Navier-Stokes (RANS) type simulation framework where a simple Buckingham-Π analysis [46] would require a functional form of the parametric space that is given by

$$R = G(P_i), \tag{9}$$

where R is the parameter of interest such as the flow response, $G(\cdot)$ is the functional response with P_i being the independent parameter ranging from $i = 0$ to $i = N$ where N is the total number of morphological and fluid parameters as used in the conventional Buckingham-Π analysis. To fully characterise R the effect of the most important parameters P_i must be accounted for, and since this is a large parameter space problem, it is computationally infeasible to explore such a wide state space. It is important to note that it is not readily clear which parameters are most important as drawing such a conclusion would require understanding the response function G at least to the first-order, which is currently poorly understood. This makes predicting flows in complex urban areas computationally expensive and has remained a challenge even when it comes to relatively simplified RANS-style simulations subject to varying inflow wind incidence.

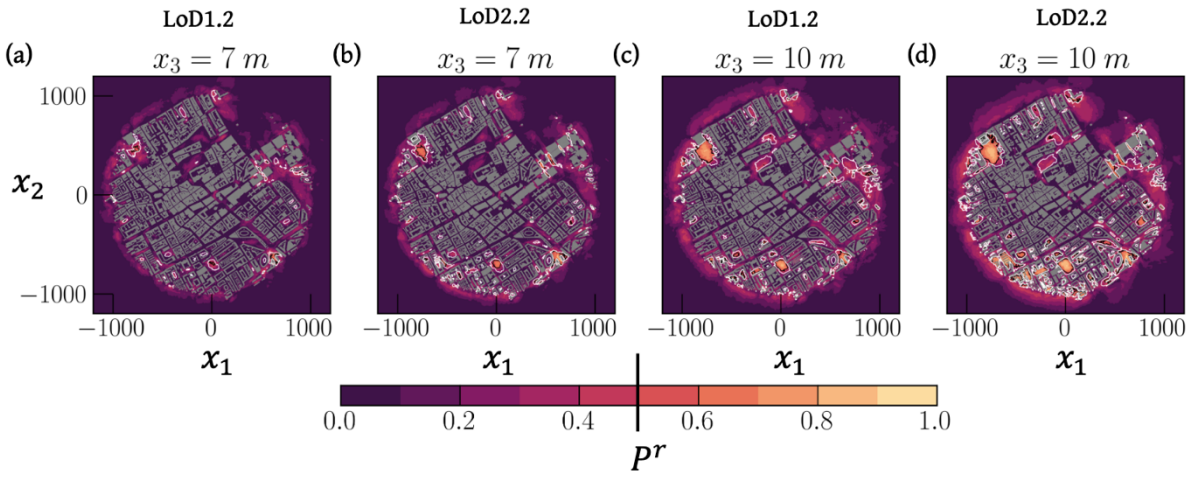

Figure 7: Comparison of the risk metric as a function of the two LoDs considered in this study at 7m and 10m above the ground ($x_3 = 0$). Here, the solid black line marks the contour for $P^r = 0.5$, and the solid white line marks the contour for $P_k^r = 0.5$, which is the probability that $k^* > \beta \equiv 0.05$.

5. Conclusions

In this report, we presented the effect of a systematic method to characterize one of the many urban morphology parameters i.e., building geometry level of detail (LoD) on wind prediction capabilities of the RANS computational approach using a wind-incidence angular resolution of 1°. We found that lower LoD, specifically LoD1.2 tends to over-predict the wind speed within the urban area when compared to LoD2.2 due to a single height attributed to the building footprint in LoD1.2. The overall differences between LoD1.2 and LoD2.2 for the directionally averaged wind speed are not large (less than 10%) when compared against each other. However, a systematic under-prediction is observed in LoD1.2 when the joint exceedance probability of velocity and turbulence levels is considered.

Based on our observations and data, any generalizations of the overall urban morphological response to the inflow conditions must be made with care as the transfer function between the input and output is not known a priori. Since the parameters required to characterize urban morphology require a large number of metrics, concluding the universality of a few parameters can be speculative at best, if not entirely problematic. Our data suggest that even small changes in the geometric characterization of the buildings introduce systematic differences in the risk parameters. Thus, universality regarding relatively more complex urban morphological response requires a detailed investigation and more comprehensive numerical experiments.

References

[1] B. Blocken, “Computational Fluid Dynamics for urban physics: Importance, scales, possibilities, limitations and ten tips and tricks towards accurate and reliable simulations,” Build Environ, vol. 91, pp. 219–245, Sep. 2015, doi: 10.1016/j.buildenv.2015.02.015.

[2] B. Güneralp, M. Reba, B. U. Hales, E. A. Wentz, and K. C. Seto, “Trends in urban land expansion, density, and land transitions from 1970 to 2010: a global synthesis,” *Environmental Research Letters*, vol. 15, no. 4, p. 44015, Mar. 2020.

[3] R. I. McDonald *et al.*, “Research gaps in knowledge of the impact of urban growth on biodiversity,” *Nat Sustain*, vol. 3, no. 1, pp. 16–24, Dec. 2019, doi: 10.1038/s41893-019-0436-6.

[4] G. Pomaranzi, L. Amerio, P. Schito, G. Lamberti, C. Gorlé, and A. Zasso, “Wind tunnel pressure data analysis for peak cladding load estimation on a high-rise building,” *Journal of Wind Engineering and Industrial Aerodynamics*, vol. 220, p. 104855, Jan. 2022, doi: 10.1016/j.jweia.2021.104855.

[5] M. F. Ciarlatani, Z. Huang, D. Philips, and C. Gorlé, “Investigation of peak wind loading on a high-rise building in the atmospheric boundary layer using large-eddy simulations,” *Journal of Wind Engineering and Industrial Aerodynamics*, vol. 236, p. 105408, May 2023, doi: 10.1016/j.jweia.2023.105408.

[6] J. Hochschild and C. Gorlé, “Design and demonstration of a sensing network for full-scale wind pressure measurements on buildings,” *Journal of Wind Engineering and Industrial Aerodynamics*, vol. 250, p. 105760, 2024, doi: https://doi.org/10.1016/j.jweia.2024.105760.

[7] J. Hochschild and C. Gorlé, “Comparison of measured and LES-predicted wind pressures on the Space Needle,” *Journal of Wind Engineering and Industrial Aerodynamics*, vol. 249, p. 105749, 2024, doi: https://doi.org/10.1016/j.jweia.2024.105749.

[8] D. Fowler *et al.*, “A chronology of global air quality: The development of global air pollution,” *Philosophical Transactions of the Royal Society A: Mathematical, Physical and Engineering Sciences*, vol. 378, no. 2183, Oct. 2020, doi: 10.1098/RSTA.2019.0314.

[9] T. Wolf, L. H. Pettersson, and I. Esau, “A very high-resolution assessment and modelling of urban air quality,” *Atmos Chem Phys*, vol. 20, no. 2, pp. 625–647, Jan. 2020, doi: 10.5194/ACP-20-625-2020.

[10] C. Nagl, I. Buxbaum, S. Bohmer, N. Ibesich, and H. R. Mendoza, “Air Quality and urban traffic in the EU: best practices and possible solutions,” 2018. doi: https://www.europarl.europa.eu/RegData/etudes/STUD/2018/604988/IPOL_STU(2018)604988_EN.pdf.

[11] M. Elsayed and M. Mohamed, “The impact of airspace regulations on unmanned aerial vehicles in last-mile operation,” *Transp Res D Transp Environ*, vol. 87, p. 102480, Oct. 2020, doi: 10.1016/j.trd.2020.102480.

[12] S. Cui, Y. Yang, K. Gao, H. Cui, and A. Najafi, “Integration of UAVs with public transit for delivery: Quantifying system benefits and policy implications,” *Transp Res Part A Policy Pract*, vol. 183, p. 104048, May 2024, doi: 10.1016/j.tra.2024.104048.

[13] C. Lemardelé, M. Estrada, L. Pagès, and M. Bachofner, “Potentialities of drones and ground autonomous delivery devices for last-mile logistics,” *Transportation Research Part E*, vol. 149, pp. 1366–5545, 2021, doi: 10.1016/j.tre.2021.102325.

[14] B. Galkin, J. Kibilda, and L. A. DaSilva, “UAVs as Mobile Infrastructure: Addressing Battery Lifetime,” *IEEE Communications Magazine*, vol. 57, no. 6, pp. 132–137, Jun. 2019, doi: 10.1109/MCOM.2019.1800545.

[15] B. Blocken, “50 years of computational wind engineering: past, present and future,” *Journal of Wind Engineering and Industrial Aerodynamics*, vol. 129, pp. 69–102, 2014.

[16] G. Boeing, “Measuring the complexity of urban form and design,” *URBAN DESIGN International*, vol. 23, no. 4, pp. 281–292, Nov. 2018, doi: 10.1057/s41289-018-0072-1.

[17] F. Biljecki and Y. S. Chow, “Global Building Morphology Indicators,” *Comput Environ Urban Syst*, vol. 95, p. 101809, Jul. 2022, doi: 10.1016/J.COMPENVURBSYS.2022.101809.

[18] A. Labetski, S. Vitalis, F. Biljecki, K. Arroyo Ohori, and J. Stoter, “3D building metrics for urban morphology,” *International Journal of Geographical Information Science*, vol. 37, no. 1, pp. 36–67, Jan. 2023, doi: 10.1080/13658816.2022.2103818.

[19] T.-O. Hågbo, K. Erik Teigen Giljarhus, and B. Helge Hjertager, “Influence of geometry acquisition method on pedestrian wind simulations,” 2021, doi: 10.1016/j.jweia.2021.104665.

[20] T. O. Hågbo and K. E. T. Giljarhus, “Pedestrian Wind Comfort Assessment Using Computational Fluid Dynamics Simulations With Varying Number of Wind Directions,” *Front Built Environ*, vol. 8, p. 858067, Jul. 2022, doi: 10.3389/FBUIL.2022.858067/BIBTEX.

[21] T.-O. Hågbo and K. E. T. Giljarhus, “Sensitivity of urban morphology and the number of CFD simulated wind directions on pedestrian wind comfort and safety assessments,” *Build Environ*, vol. 253, p. 111310, Apr. 2024, doi: 10.1016/j.buildenv.2024.111310.

[22] B. Wang, S. Sun, and M. Duan, “Wind potential evaluation with urban morphology - A case study in Beijing,” *Energy Procedia*, vol. 153, pp. 62–67, 2018, doi: https://doi.org/10.1016/j.egypro.2018.10.078.

[23] C. Garcìa-Sánchez, S. Vitalis, I. Paden, and J. Stoter, “THE IMPACT OF LEVEL OF DETAIL IN 3D CITY MODELS FOR CFD-BASED WIND FLOW SIMULATIONS,” *The International Archives of the Photogrammetry, Remote Sensing and Spatial Information Sciences*, vol. XLVI-4/W4-2021, pp. 67–72, 2021, doi: 10.5194/isprs-archives-XLVI-4-W4-2021-67-2021.

[24] Q. Cao, Q. Luan, Y. Liu, and R. Wang, “The effects of 2D and 3D building morphology on urban environments: A multi-scale analysis in the Beijing metropolitan region,” *Build Environ*, vol. 192, p. 107635, Apr. 2021, doi: 10.1016/j.buildenv.2021.107635.

[25] T. F. Alemayehu and G. T. Bitsuamlak, “Autonomous urban topology generation for urban flow modelling,” *Sustain Cities Soc*, vol. 87, p. 104181, Dec. 2022, doi: 10.1016/j.scs.2022.104181.

[26] M. Fleischmann, O. Romice, and S. Porta, “Measuring urban form: Overcoming terminological inconsistencies for a quantitative and comprehensive morphologic analysis of cities,” *EPB: Urban Analytics and City Science*, vol. 48, no. 8, pp. 2133–2150, 2021, doi: 10.1177/2399808320910444.

[27] J. Hang, M. Sandberg, and Y. Li, “Effect of urban morphology on wind condition in idealized city models,” *Atmos Environ*, vol. 43, no. 4, pp. 869–878, Feb. 2009, doi: 10.1016/J.ATMOSENV.2008.10.040.

[28] M. Carpentieri and A. G. Robins, “Influence of urban morphology on air flow over building arrays,” *Journal of Wind Engineering and Industrial Aerodynamics*, vol. 145, pp. 61–74, Oct. 2015, doi: 10.1016/J.JWEIA.2015.06.001.

[29] O. Palusci, P. Monti, C. Cecere, H. Montazeri, and B. Blocken, “Impact of morphological parameters on urban ventilation in compact cities: The case of the Tuscolano-Don Bosco district in Rome,” 2021, doi: 10.1016/j.scitotenv.2021.150490.

[30] M. Karimimoshaver, R. Khalvandi, and M. Khalvandi, “The effect of urban morphology on heat accumulation in urban street canyons and mitigation approach,” *Sustain Cities Soc*, vol. 73, p. 103127, Oct. 2021, doi: 10.1016/J.SCS.2021.103127.

[31] F. Biljecki, H. Ledoux, and J. Stoter, “An improved LOD specification for 3D building models,” *Comput Environ Urban Syst*, vol. 59, pp. 25–37, Sep. 2016, doi: 10.1016/j.compenvurbsys.2016.04.005.

[32] J. van der Vaart, J. Stoter, A. Diakité, F. Biljecki, K. A. Ohori, and A. Hakim, “Assessment of the LoD Specification for the Integration of BIM-Derived Building Models in 3D City Models,” *Lecture Notes in Geoinformation and Cartography*, pp. 171–191, 2024, doi: 10.1007/978-3-031-43699-4_11/FIGURES/14.

[33] B. E. Launder and D. B. Spalding, “The numerical computation of turbulent flows,” *Comput Methods Appl Mech Eng*, vol. 3, no. 2, pp. 269–289, Mar. 1974, doi: 10.1016/0045-7825(74)90029-2.

[34] S. Patankar, *Numerical Heat Transfer and Fluid Flow*, 1st edition. Boca Raton, Florida: CRC Press, 1980.

[35] H. G. Weller, G. Tabor, H. Jasak, and C. Fureby, “A tensorial approach to computational continuum mechanics using object-oriented techniques,” *Computer in Physics*, vol. 12, no. 6, pp. 620–631, Jan. 1998.

[36] D. H. P. C. (DHPC), “DelftBlue Supercomputer (Phase 2),” 2024.

[37] R. Peters, B. Dukai, S. Vitalis, J. van Liempt, and J. Stoter, “Automated 3D Reconstruction of LoD2 and LoD1 Models for All 10 Million Buildings of the Netherlands,” *Photogramm Eng Remote Sensing*, vol. 88, no. 3, pp. 165–170, Mar. 2022, doi: 10.14358/PERS.21-00032R2.

[38] I. Pađen, C. García-Sánchez, and H. Ledoux, “Towards automatic reconstruction of 3D city models tailored for urban flow simulations,” *Front Built Environ*, vol. 8, p. 899332, Aug. 2022, doi: 10.3389/FBUIL.2022.899332/BIBTEX.

[39] I. Pađen, R. Peters, C. García-Sánchez, and H. Ledoux, “Automatic high-detailed building reconstruction workflow for urban microscale simulations,” *Build Environ*, vol. 265, p. 111978, 2024.

[40] J. Wieringa, “Updating the Davenport roughness classification,” *Journal of Wind Engineering and Industrial Aerodynamics*, vol. 41, no. 1–3, pp. 357–368, Oct. 1992, doi: 10.1016/0167-6105(92)90434-C.

[41] J. Franke, A. Hellsten, K. H. Schlunzen, and B. Carissimo, *The COST 732 best practice guideline for CFD simulation of flows in urban environment: A summary.*, vol. 44. 2011.

[42] I. B. Celik, U. Ghia, P. J. Roache, and C. J. Freitas, “Procedure for estimation and reporting of uncertainty due to discretization in CFD applications,” *Journal of fluids Engineering-Transactions of the ASME*, vol. 130, no. 7, 2008.

[43] I. B. Celik, U. Ghia, P. J. Roache, and C. J. Freitas, “Procedure for estimation and reporting of uncertainty due to discretization in CFD applications,” *Journal of fluids Engineering-Transactions of the ASME*, vol. 130, no. 7, 2008.

[44] T. V Lawson, “The widn content of the built environment,” *Journal of Wind Engineering and Industrial Aerodynamics*, vol. 3, no. 2–3, pp. 93–105, Jan. 1978, doi: 10.1016/0167-6105(78)90002-8.

[45] J. van der Vaart, J. Stoter, A. Diakité, F. Biljecki, K. A. Ohori, and A. Hakim, “Assessment of the LoD Specification for the Integration of BIM-Derived Building Models in 3D City Models,” *Lecture Notes in Geoinformation and Cartography*, pp. 171–191, 2024, doi: 10.1007/978-3-031-43699-4_11/FIGURES/14.

[46] E. Buckingham, “On Physically Similar Systems; Illustrations of the Use of Dimensional Equations,” *Phys. Rev.*, vol. 4, no. 4, pp. 345–376, Oct. 1914, doi: 10.1103/PhysRev.4.345.

Annex A

To better quantify the sensitivity of the risk map parameters, we compare the effect of risk map prediction for the two LoDs considered in this paper. We use the TUD-campus case for which the risk map is calculated. In the Figures below, the risk map calculated for LoD1.2 is compared against the risk map calculated for LoD2.2 with increasing values of α and β. For increasing values of α, the region predicted to be above the 50%-mark shrinks, which is not surprising since the area corresponding to a relatively larger non-dimensional velocity shrinks. For the same value of α and increasing values of β, a similar reduction in the risk map is observed since the regions with relatively large non-dimensional velocity and TKE shrink in size. Figures 8-14 exhibit a constant under prediction by LoD1.2 in the risk region when compared to LoD2.2, further supporting the utility of the joint probability distribution as a useful metric to quantify the similarities and differences observed for this case.

For small values of $\beta < 0.04$, the risk map classifies most of the area as high-risk mainly because of the smallness of the parameter such that all grid points return a positive value. This is especially true for $\alpha < 0.4$ where most if not all of the area presented in the figures below is classified as high-risk. Since small values of β introduce this consistent bias, the choice for $\alpha < 0.4$ and $\beta < 0.08$ was made in this work to quantify the differences between the two LoDs. It is important to remark that this choice must be made with care and is not a generalisation for other urban geometries and only serves to compare the two different LoDs.

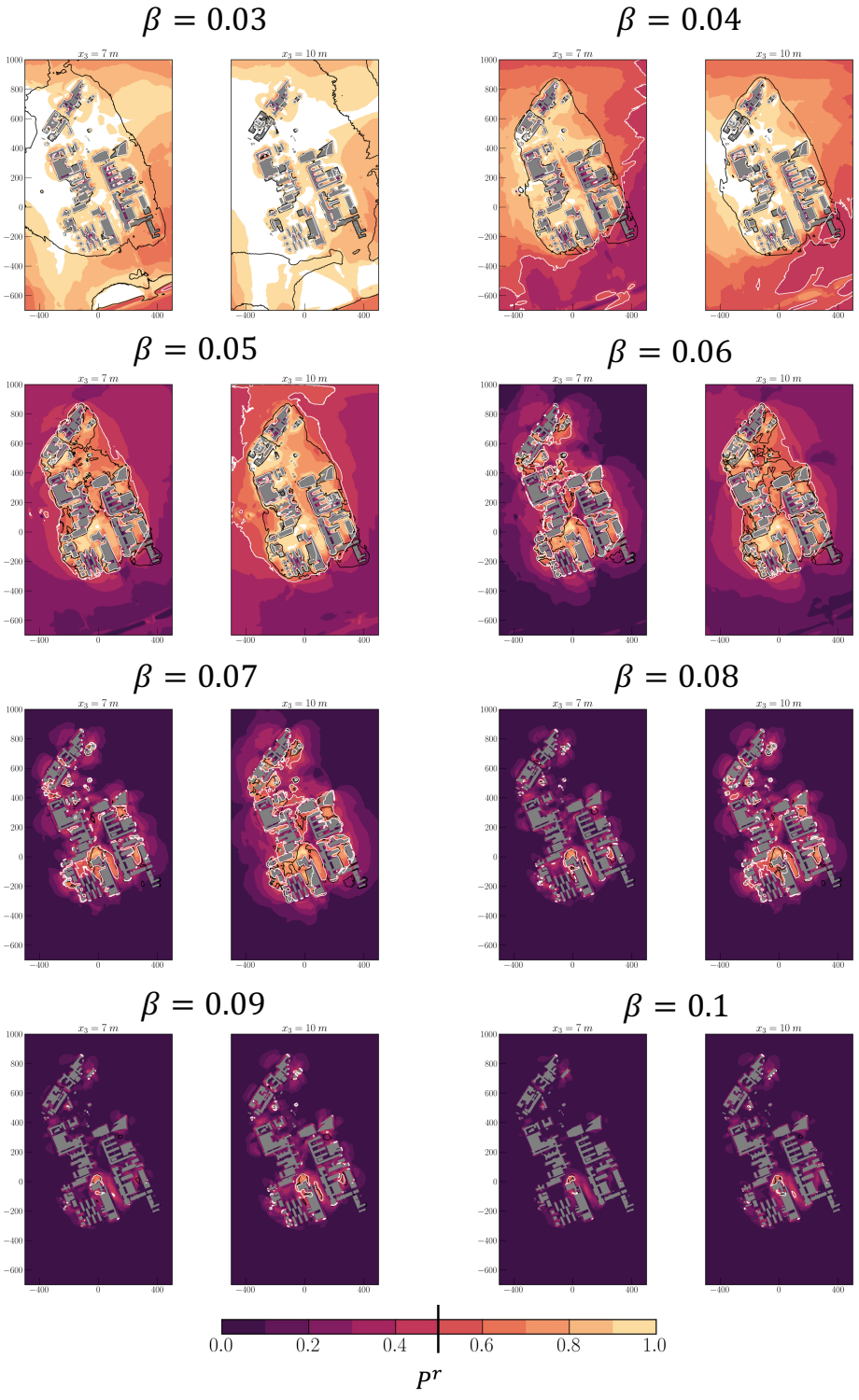

Figure 8: Comparison of the risk map for $\alpha = 0.1$ with varying values of β. The black solid lines correspond to LoD1.2 and the white solid lines correspond to LoD2.2. The colours mark the risk map associated with LoD2.2 while the gray region corresponds to LoD1.2.

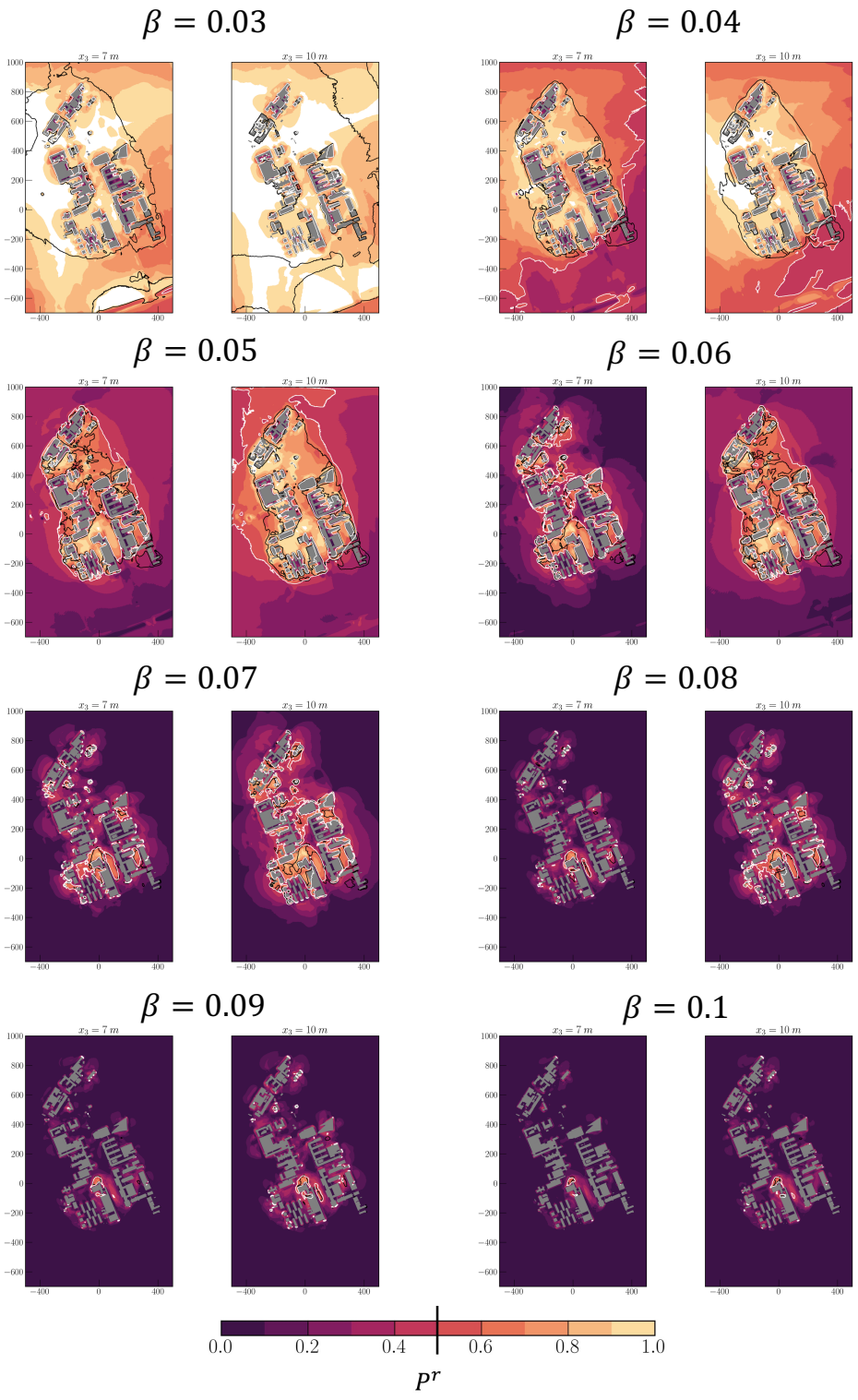

Figure 9: Same as Figure 8 and α = 0.2.

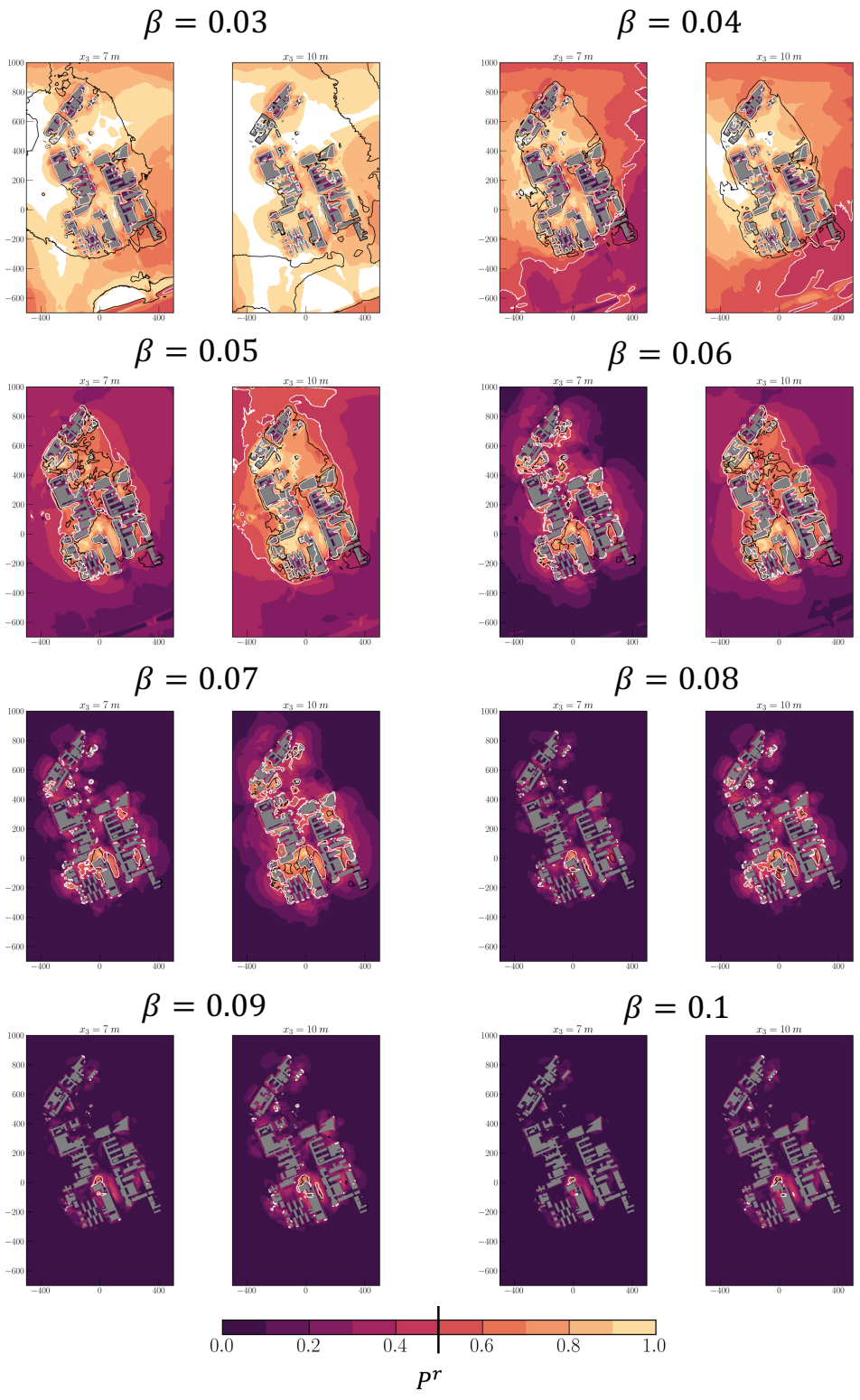

Figure 10: Same as Figure 8 and α = 0.3.

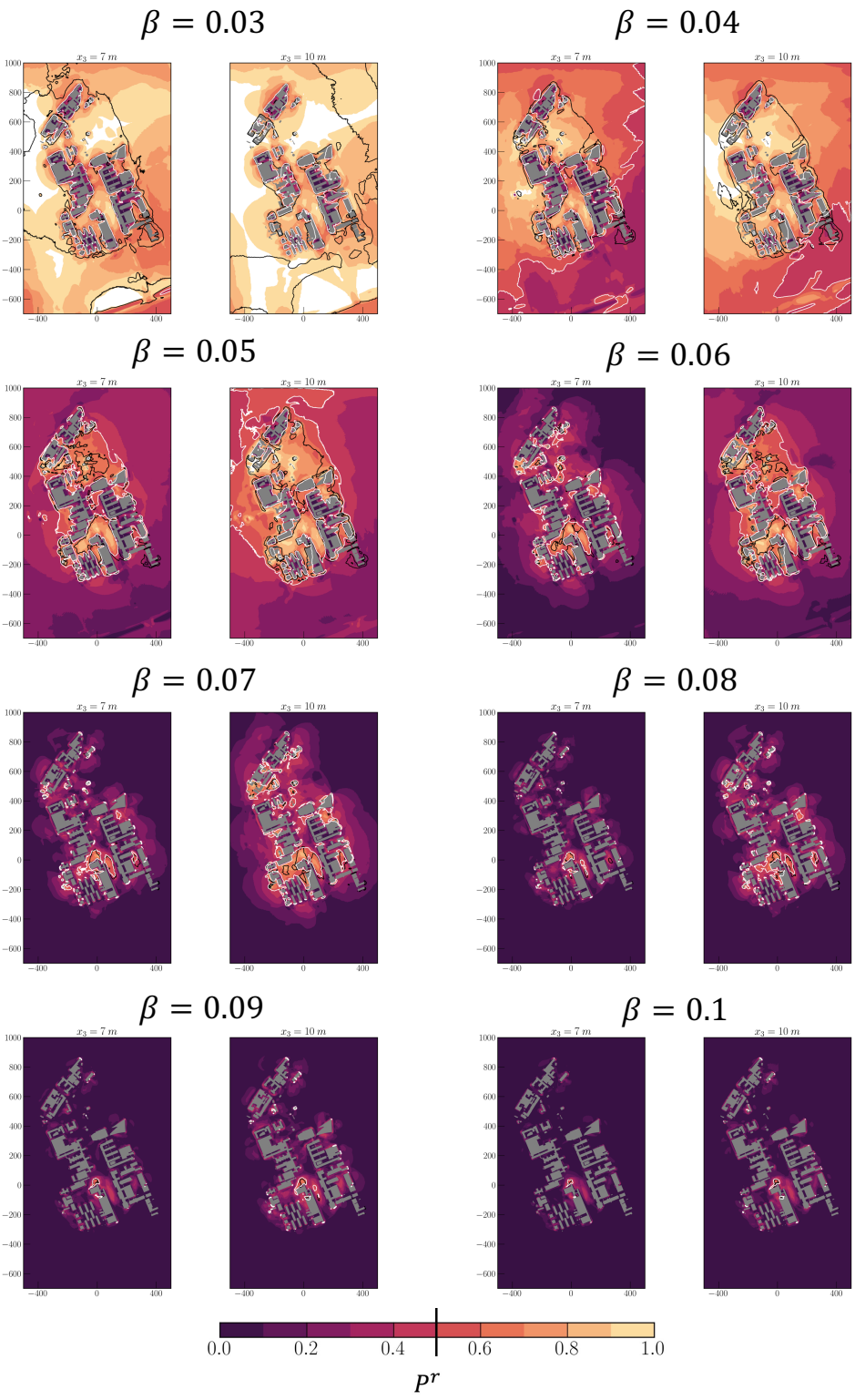

Figure 11: Same as Figure 8 and α = 0.4.

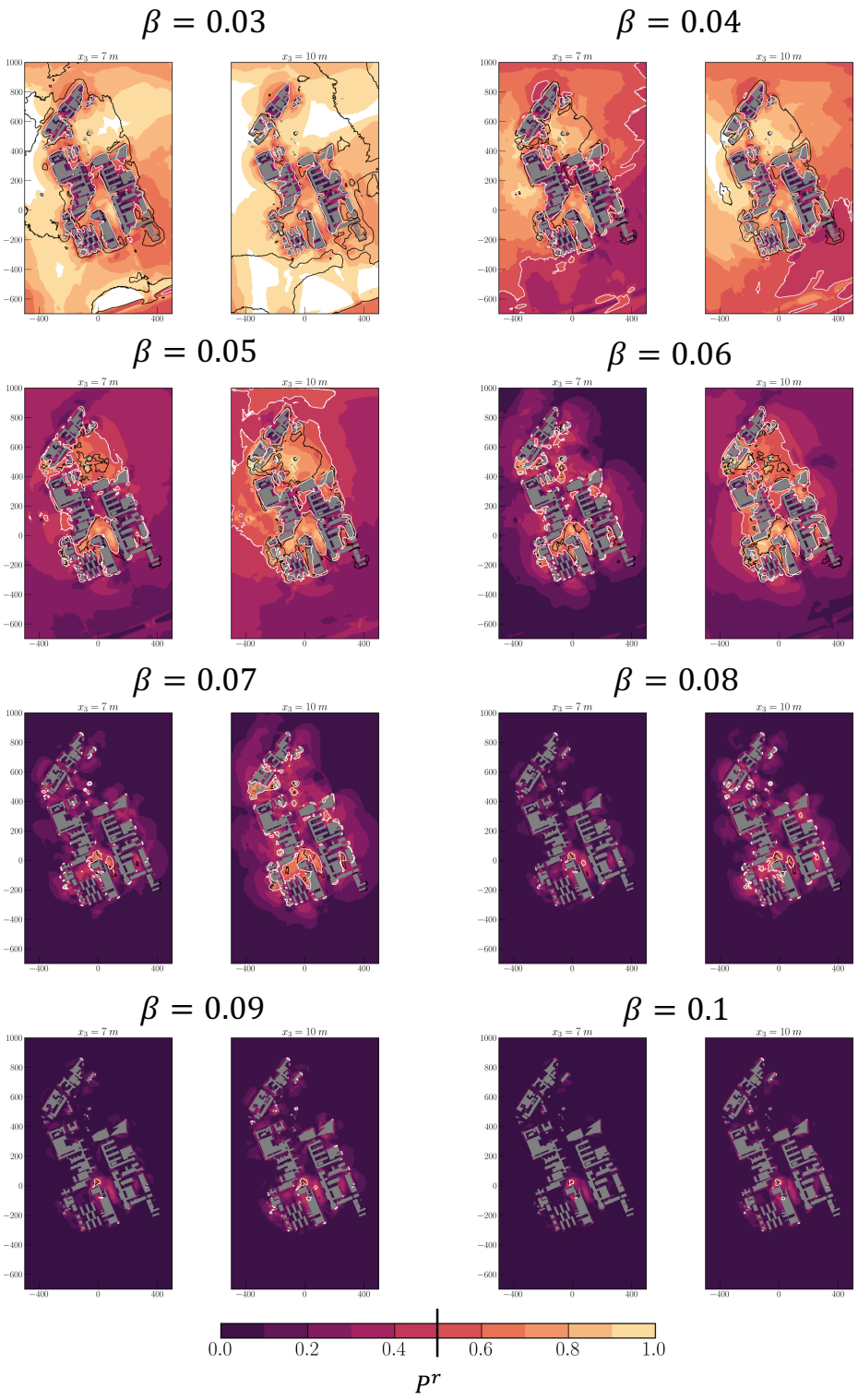

Figure 12: Same as Figure 8 and α = 0.5.

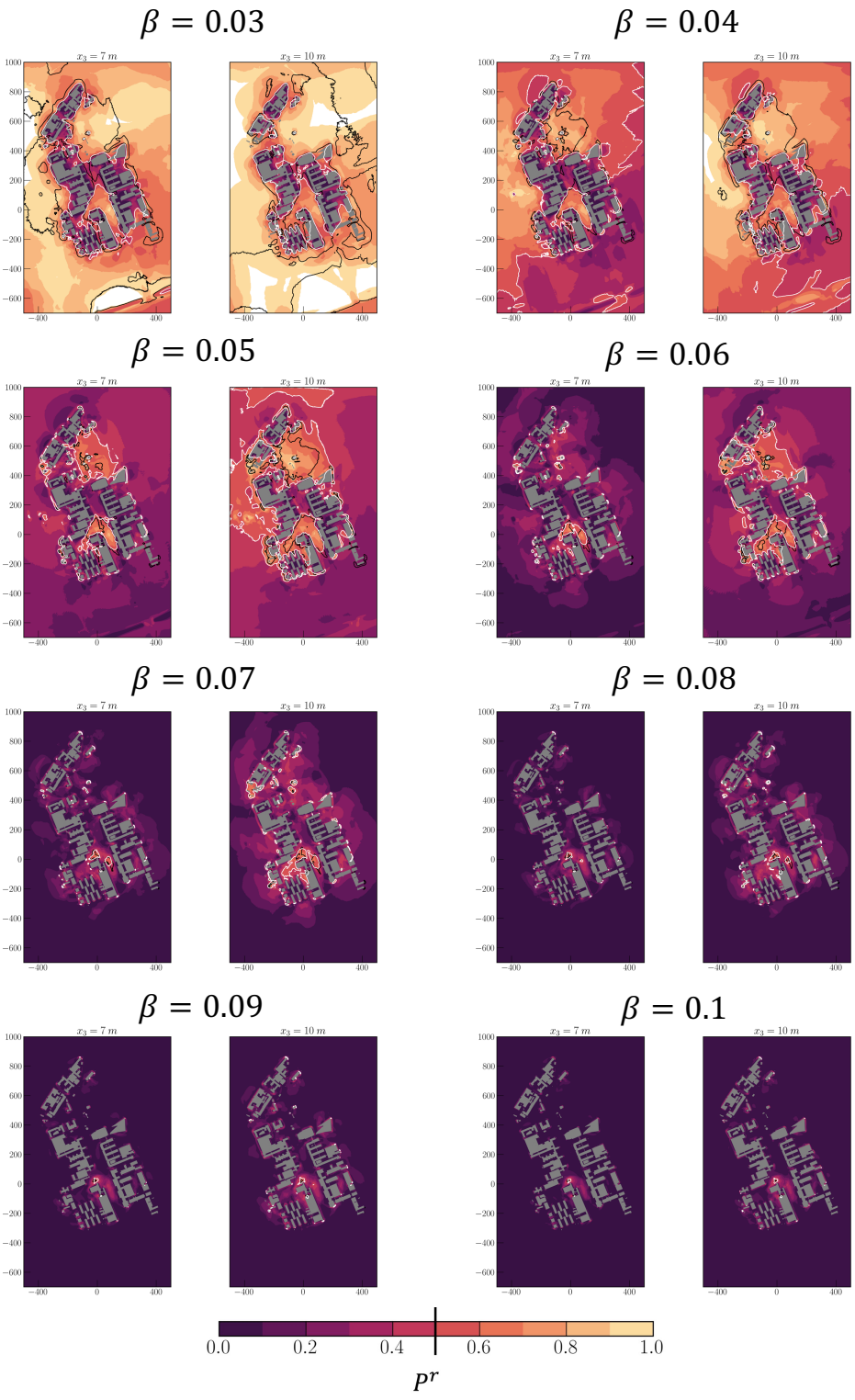

Figure 13: Same as Figure 8 and α = 0.6.

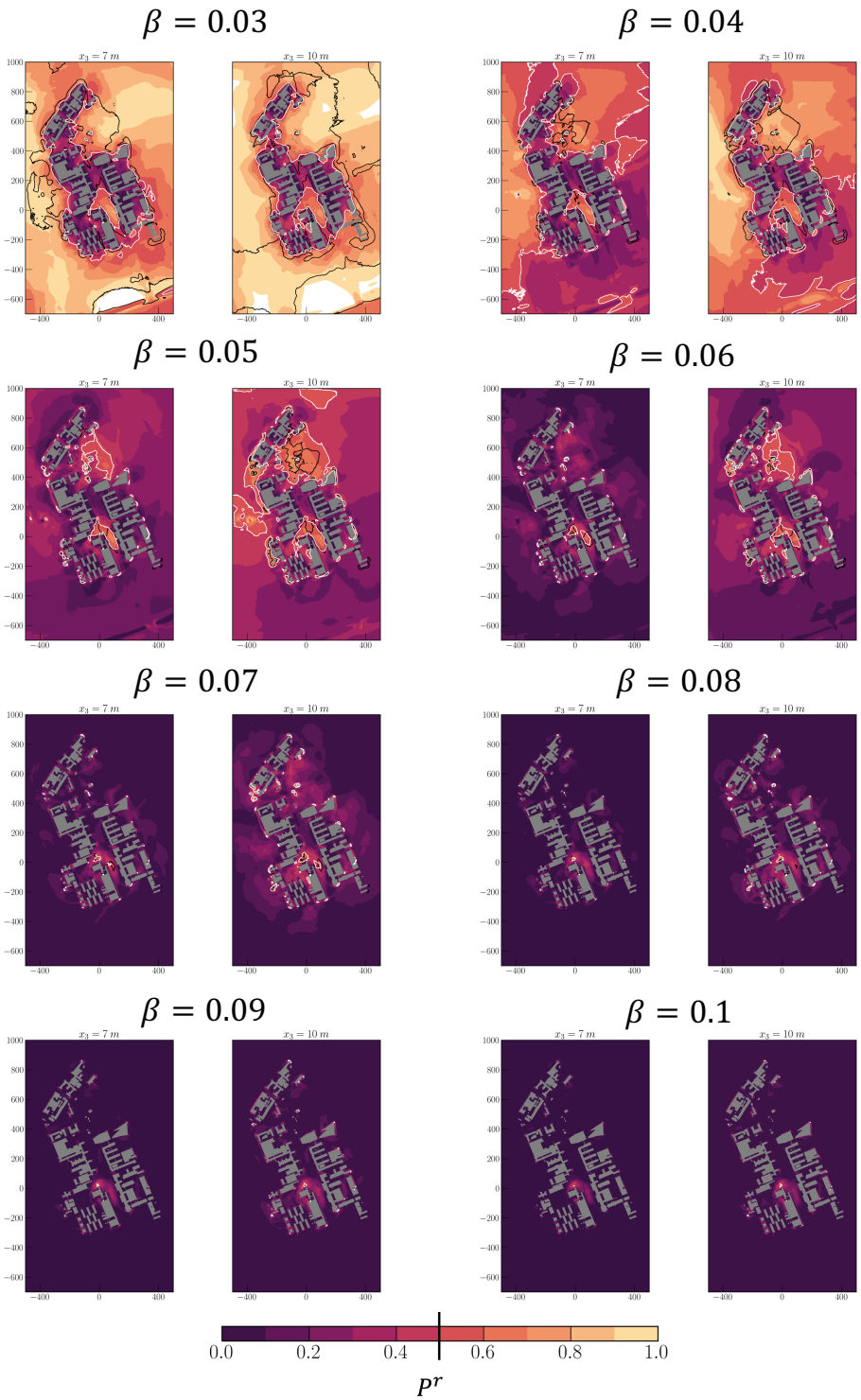

Figure 14: Same as Figure 8 and α = 0.7.